Springer

Acta Mechanica Sinica

CrossMark click for updates

• RESEARCH PAPER •

Acta Mech. Sin., Vol. 40, 323630 (2024)
https://doi.org/10.1007/s10409-024-23630-x

Temperature and heat flux bounds of convection driven by non-uniform internal heating

Liangbing Chen, An-Kang Gao*, Zimo Liao, Zhenhua Wan, and Nansheng Liu*

Department of Modern Mechanics, University of Science and Technology of China, Hefei 230026, China

Received January 16, 2024; accepted January 28, 2024; published online June 11, 2024

Convection driven by a spatially non-uniform internal heat source between two horizontal isothermal walls is studied by theoretical analysis and numerical simulation, in order to explore the bounds of the temperature and the vertical heat flux. Specifically, the rigorous lower bound of the weighted average temperature $\langle QT \rangle$ is derived analytically, by decomposing the temperature field into a background profile and a fluctuation part. This bound obtained for the first time to consider non-uniform heat sources is found to be compatible with the existing bound obtained in uniform internal heat convection. Of physical importance, an analytical relationship is derived as an inequality connecting $\langle QT \rangle$ and the average vertical heat flux $\langle wT \rangle$, by employing the average heat flux on the bottom wall (q_b) as an intermediary variable. It clarifies the intrinsic relation between the lower bound of $\langle QT \rangle$ and the upper bound of $\langle wT \rangle$, namely, these two bounds are essentially equivalent providing an easy way to obtain one from another. Furthermore, the analytical bounds are extensively demonstrated through a comprehensive series of direct numerical simulations.

Internally heated convection, Nonuniform internal heat source, Analytical bounds, Background method

Citation: L. Chen, A.-K. Gao, Z. Liao, Z. Wan, and N. Liu, Temperature and heat flux bounds of convection driven by non-uniform internal heating, Acta Mech. Sin. **40**, 323630 (2024), https:// doi.org/10.1007/s10409-024-23630-x

1. Introduction

Internally heated convection (IHC) is widely encountered in nature and industry and is therefore of great scientific and practical importance. The internal heat source originates from various physical and chemical processes [1, 2], such as the decay of radioactive elements in mantle convection [3], the absorption of stellar radiant by the planetary atmosphere [4, 5], and the Joule heat generated by the electric current in liquid metal batteries [6, 7]. Understanding the IHC is essential in explaining these natural phenomena as well as guiding thermal designs and management of industrial equipments.

As a fundamental model problem, IHC has attracted a vast variety of research efforts including experimental measurements [8-11] and numerical simulations [12-18], which intend to pave the way for a comprehensive understanding of its intriguing fluid dynamics. When the flow is maintained static in an IHC which has the same temperature fixed on the top and the bottom walls, the temperature interior of the fluid layer is known to be always higher than the wall temperature [14], resulting in a stable thermal stratification near the bottom wall whereas an unstable one near the top wall. Goluskin [19] performed instability analyses for the IHC with a constant heat source (Uniformly Internally Heated Convection, UIHC), and found that the critical Rayleigh numbers for the linear instability and the energy instability are $R_L = 37325.2$ and $R_E = 26926.6$, respectively. Therefore, when the Rayleigh number R is large enough, thermal convection occurs inevitably. In the UIHC, the top thermal boundary layer is much thinner than the bottom one, which reflects the up-down asymmetry of the systems [19] and more heat escaping through the top wall than the bottom one [10, 13]. The momentum and heat generated in the un-

*Corresponding authors. E-mail addresses: ankanggao@ustc.edu.cn (An-Kang Gao); lns@ustc.edu.cn (Nansheng Liu)

Executive Editor: Chao Sun

stable region are transferred to the stable region when the upper layer pulls cold eddies off the bottom boundary layer by shearing forces, which is the so-called penetrative convection [20, 21]. Penetrative convection essentially changes the flow dynamics and energy transport characteristic in the UIHC, which is drastically different from the classical Rayleigh-Bérnard Convection (RBC) [22-24] where the convection is driven purely by the heated bottom wall.

In the UIHC, as argued by Goluskin and Spiegel [14], the average temperature $\langle T\rangle$ and the vertical heat-flux $\langle wT\rangle$ are better diagnostic quantities than the Nusselt number which is extensively analyzed in the RBC. Here, w and T are the dimensionless vertical velocity component and the temperature, respectively. The bracket $\langle\cdot\rangle$ denotes the temporal and spatial averaging. Numerical results indicate that the average temperature $\langle T\rangle$ has a scaling of $R^{-1/5}$ in a broad high-R regime ($0.01 \le Pr \le 100$, $10^4 \le R \le 5\times10^{10}$) [13, 18]. In rigorous theoretical analysis, the asymptotic behaviours or bounds of the $\langle T\rangle$ and $\langle wT\rangle$ are also obtained [25-31]. The first analytical bound of $\langle T\rangle$ in the UIHC is reported by Lu et al. [31]. Recently, a series of bounds of $\langle T\rangle$ and $\langle wT\rangle$ have been reported to obtain more accurate flow diagnosis in the UIHC, as listed in Table 1 [14, 31-35].

In the pioneering work of Lu et al. [31], a background method [36, 37], which decomposes the flow into a background profile and a fluctuation part, is introduced in the study of the UIHC. By constructing feasible solutions to a convex variational problem, Arslan et al. [32] found an R-dependent scaling of $\langle wT\rangle \le 2^{-21/5}R^{1/5}$, which improves the uniform bound of $\langle wT\rangle \le 1/2$ [14] in the range of $R < 65536$. With an improvement of the background profile in the boundary layers, Kumar et al. [34] found a different bound of $\langle wT\rangle \le 1/2 - 3.29R^{1/5}\exp\left(-17.58R^{3/5}\right)$ for $R \ge 31$. For $R\to\infty$, this bound increases to its asymptotic value of $1/2$. Nevertheless, because the magnitude of the additional negative term decays exponentially, this correction term has a maximum value of approximately 10^{-60} over the entire range of R, rendering that the bound is not so valuable in practice. The most recent work of Arslan et al. [33] established a bound of $\langle wT\rangle$ for the infinite Pr showing that $\langle wT\rangle$ approaches $1/2$ at a rate of R^{-2} as $R\to\infty$.

As the analytical bounds discussed above are limited to the UIHC, the present work is dedicated to exploring the analytical bounds of the non-uniformly internally heated convection (NUIHC) having a positive internal heat source $Q \ge 0$, which is more common in nature and industry [3,5], however, rarely concerned up to date. Specifically, by using the background method, we derived the analytical rigorous bounds of the $\langle QT\rangle$ and $\langle wT\rangle$ that highly depend on the distribution of heat sources Q and control parameter R. Extensive numerical simulations have been considered for different heat source distributions to validate these theoretical results.

The rest of this paper is organized as follows: Section 2 introduces the governing equations and flow model. Section 3 presents the concise derivations and relevant discussions of the theoretical bounds. Section 4 presents the numerical results and analysis of the effect of heat sources on flow structure as well as the demonstration of the theoretical bounds. Finally, a brief conclusion is provided in Sect. 5. The detail of the derivations of theoretical bounds and code validation is described in Appendix A and Appendix B.

2. Problem description

Figure 1 shows a classical model of the NUIHC happening in a fluid layer confined vertically between two horizontal walls, with the top and bottom walls of a distance d^* and fixed at the same temperature T_c^*. The convection driven by an internal heat source Q^* is considered for the fluid of constant kinematic viscosity ν^*, thermal diffusivity κ^*, coefficient of thermal expansion α^*, density ρ^*, and specific heat capacity c_p^*. g^* is the gravitational acceleration pointing along the negative z-direction. Here, the superscript $*$ is used to denote the dimensional variables.

By adopting the Oberbeck-Boussinesq approximation, the dimensionless governing equations for the NUIHC are given as

$$\nabla\cdot\boldsymbol{u} = 0, \tag{1a}$$

$$\partial_t\boldsymbol{u} + \boldsymbol{u}\cdot\nabla\boldsymbol{u} + \nabla p = Pr\nabla^2\boldsymbol{u} + PrRT\boldsymbol{e}_z, \tag{1b}$$

$$\partial_t T + \boldsymbol{u}\cdot\nabla T = \nabla^2 T + Q. \tag{1c}$$

The dimensionless quantities involved in the above governing equations are obtained as follows:

$$\begin{aligned} &\boldsymbol{x} = \frac{\boldsymbol{x}^*}{d^*}, \quad t = \frac{t^*}{d^{*2}/\kappa^*}, \quad \boldsymbol{u} = \frac{\boldsymbol{u}^*}{\kappa^*/d^*},\\ &p = \frac{p^*}{\rho^*\kappa^{*2}/d^{*2}}, \quad T = \frac{T^*-T_c^*}{d^{*2}\gamma^*/(\kappa^*\rho^*c_p^*)}, \quad Q = \frac{Q^*}{\gamma^*}. \end{aligned} \tag{2}$$

Here, $\boldsymbol{x}$ and t are the dimensionless spatial coordinates and time, respectively. $\boldsymbol{u}$, p and T denote the dimensionless velocity, pressure, and temperature, respectively. Q represents

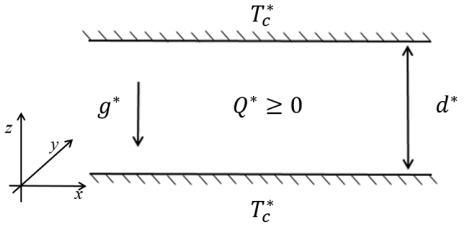

Figure 1 Flow configuration.

Table 1 Summary of bounds in the UIHC

	Ref.	Bounds
$\langle wT\rangle$	Goluskin and Spiegel [14]	$0 < \langle wT\rangle < 1/2$
	Arslan et al. [32]	$\langle wT\rangle \le 2^{-21/5}R^{1/5}$, when $R < 65536$
	Kumar et al. [34]	$\langle wT\rangle \le 1/2 - 3.29R^{1/5}\exp\left(-17.58R^{3/5}\right)$, when $R \ge 31$
	Arslan et al. [33]	$\langle wT\rangle \le 1/2 - 216R^{-2}$, when $Pr = \infty$
$\langle T\rangle$	Lu et al. [31]	$\langle T\rangle \ge 4.421R^{-1/3}$
	Lu et al. [31]	$\langle T\rangle \ge 0.810R^{-2/7}$, when $Pr = \infty$
	Whitehead and Doering [35]	$\langle T\rangle \ge 0.419(R\log R)^{-1/4}$, when $Pr = \infty$

the prescribed dimensionless heat source that has an average of $\langle Q\rangle = 1$, with γ^* being the averaged heat source. The two key dimensionless parameters, the Prandtl number Pr and the Rayleigh number R (or Rayleigh Robert number), are defined as

$$Pr = \frac{\nu^*}{\kappa^*}, \quad \text{and} \quad R = \frac{g^*\alpha^* d^{*5}\gamma^*}{\rho^* c_p^* \nu^* \kappa^{*2}}. \tag{3}$$

The top and bottom walls are considered to have the no-slip and isothermal conditions with the non-dimensional velocity and temperature fixed as

$$\boldsymbol{u}\big|_{z=0,1} = \boldsymbol{0}, \quad \text{and} \quad T\big|_{z=0,1} = 0. \tag{4}$$

The average heat fluxes on the bottom (q_b) and top (q_t) walls are obtained by

$$q_b = \frac{\partial \overline{T}}{\partial z}\Big|_{z=0}, \quad q_t = -\frac{\partial \overline{T}}{\partial z}\Big|_{z=1}. \tag{5}$$

Because of the conservation constraint of the internal energy, there is $q_t + q_b = \langle Q\rangle = 1$.

In the following, theoretical and numerical analyses are performed for the statistically stationary convection, in the context of temporal-horizontal averaging ($\overline{f}$) and temporal-spatial averaging ($\langle f\rangle$) that are defined for a given variable $f(\boldsymbol{x},\tau)$ as follows:

$$\overline{f}(z) = \lim_{t\to\infty}\frac{1}{tL_xL_y}\int_0^t \mathrm{d}\tau \int_\Omega f(\boldsymbol{x},\tau)\mathrm{d}x\mathrm{d}y, \tag{6a}$$

$$\langle f\rangle = \frac{1}{d}\int_0^d \overline{f}(z)\mathrm{d}z, \tag{6b}$$

where the horizontal domain is represented by $\Omega = [0, L_x]\times[0, L_y]$, with L_x and L_y being the domain sizes in the x- and y-directions, respectively. Following Kumar et al. [34], L_x and L_y are considered to be sufficiently large so that the effect of very low-frequency fluid motions and large-scale structures can be ignored and the convective flow is assumed to be periodic in the horizontal (x- and y-) directions.

3. Theoretical analysis

3.1 Lower bound of $\sqrt{\langle T^2\rangle}$

As detailed in Appendix A, we extend the approach adopted by Lu et al. [31] for the UIHC to the present NUIHC and derive the bound of the weighted average temperature $\langle QT\rangle$ at a finite Prandtl number, which reads

$$\langle QT\rangle \ge \alpha g(1) - g(\alpha) - \alpha R^{-\frac{1}{3}}, \tag{7}$$

where

$$\alpha = 1 - 4R^{-\frac{1}{3}}, \tag{8a}$$

$$g(z_0) = \int_0^{z_0} h(z')\mathrm{d}z', \tag{8b}$$

$$h(z_0) = \int_0^{z_0} \overline{Q}(z')\mathrm{d}z'. \tag{8c}$$

Using the Hölder's inequality, for any $m, n > 1$ and $1/m + 1/n = 1$, one obtains

$$\langle Q^m\rangle^{1/m}\langle T^n\rangle^{1/n} \ge \langle QT\rangle.$$

Therefore, a lower bound related to the temperature is derived as

$$\langle T^m\rangle^{1/m} \ge \langle Q^n\rangle^{-1/n}[\alpha g(1) - g(\alpha) - \alpha R^{-\frac{1}{3}}]. \tag{9}$$

Obviously, one can obtained the lower bound of the root-mean-square of the temperature ($\sqrt{\langle T^2\rangle}$) easily based on Eq. (10) by setting $m = n = 2$, reading as

$$\langle T^2\rangle^{1/2} \ge \langle Q^2\rangle^{-1/2}[\alpha g(1) - g(\alpha) - \alpha R^{-\frac{1}{3}}]. \tag{10}$$

3.2 Upper bound of vertical heat flux

Taking the temporal-horizontal average of Eq. (1c), the statistically stationary convection yields

$$\frac{\mathrm{d}^2\overline{T}}{\mathrm{d}z^2} = \frac{\mathrm{d}\overline{wT}}{\mathrm{d}z} - \overline{Q}. \tag{11}$$

Integrating Eq. (11) from the bottom wall ($z = 0$) to a given vertical position z gives

$$\frac{\mathrm{d}\overline{T}}{\mathrm{d}z} = \overline{wT} - h(z) + q_b. \tag{12}$$

Further integrating Eq. (12) over z up to the top wall ($z = 1$) yields

$$q_b = -\langle wT\rangle + g(1). \tag{13}$$

Equation (13) shows that the heat flux on the bottom wall (q_b) is affected by both the Q-related term $g(1) = \int_0^1 \int_0^z \overline{Q}\mathrm{d}z'\mathrm{d}z$ and the average vertical convective heat flux $\langle wT\rangle$. When the fluid layer is maintained stationary (namely, a state of purely thermal conduction), the Q-related term $g(1)$ is in physics equivalent to q_b.

To derive the bound of the vertical heat flux, it is necessary to follow Goluskin and Spiegel [14] assuming that the horizontally averaged temperature profile $\overline{T}$ satisfies the following inequality:

$$\overline{T}(z) \le \overline{T}_{\mathrm{st}}(z, z_0) = \begin{cases} (1 - z_0)z, & 0 \le z \le z_0, \\ (1 - z)z_0, & z_0 \le z \le 1, \end{cases} \tag{14}$$

where $z_0 = 1 - q_b$. Here, $\overline{T}_{\mathrm{st}}(z, z_0)$ is the temperature profile of a stationary flow generated by a concentrated heat source at z_0. $\overline{T}_{\mathrm{st}}(z, z_0)$ and $\overline{T}(z)$ have the same heat flux on the walls if $z_0 = 1 - q_b$. Goluskin and Spiegel [14] has proved that $T \ge 0$ for $Q \ge 0$, and so Eq. (14) means that the profile of $\overline{T}$ is confined within a triangle formed by $T = 0$ and $\overline{T}_{\mathrm{st}}(z, z_0)$.

First, for the stationary state where there is $w = 0$, Eq. (11) becomes $\mathrm{d}^2\overline{T}/\mathrm{d}z^2 = -\overline{Q} \le 0$. Therefore, the term $\mathrm{d}\overline{T}/\mathrm{d}z$ decreases monotonically from q_b at $z = 0$ to $q_b - 1$ at $z = 1$. Equation (14) can be proved easily by the integration of inequality

$$q_b - 1 \le \mathrm{d}\overline{T}/\mathrm{d}z \le q_b. \tag{15}$$

Generally, near the bottom wall of IHC flows with z going to zero, the vertical velocity w has the order of $O(z^2)$, the temperature has the order of $O(z)$ and therefore $\overline{wT}$ has the order of $O(z^3)$. This situation also holds near the upper wall. From Eq. (12), one obtains $\mathrm{d}\overline{T}/\mathrm{d}z = q_b - z\overline{Q}(0) + O(z^3)$, of which the integration is $\overline{T} = q_b z - 0.5z^2\overline{Q}(0) + O(z^4)$. So, Eq. (14) is valid in an immediately neighboring domain of the wall if $\overline{Q}(0) > 0$. On the other hand, numerous numerical results support the rationality of Eq. (14) or its resultant sufficient condition Eq. (15) [38-40].

From Eq. (14), one obtains

$$\langle QT\rangle = \langle \overline{Q}\,\overline{T}\rangle + \beta \le \langle \overline{Q}\,\overline{T}_{\mathrm{st}}\rangle + \beta, \tag{16}$$

with $\beta = \langle (Q - \overline{Q})(T - \overline{T})\rangle$. By using integration by parts, the term $\langle \bar{Q}\bar{T}_{\mathrm{st}}\rangle$ is obtained as

$$\begin{aligned} \langle \overline{Q}\,\overline{T}_{\mathrm{st}}\rangle &= \int_0^{1-q_b} q_b z\overline{Q}\mathrm{d}z + \int_{1-q_b}^1 (1 - q_b)(1 - z)\overline{Q}\mathrm{d}z \\ &= (1 - q_b)g(1) - g(1 - q_b) \equiv F(q_b). \end{aligned} \tag{17}$$

Substituting Eq. (13) into Eq. (17) yields an intrinsic relation between the vertical heat flux $\langle wT\rangle$ and the $\langle QT\rangle$, given as

$$\langle QT\rangle - \beta \le F\left(g(1) - \langle wT\rangle\right). \tag{18}$$

Of physical importance, this novel inequality establishes for the first time an intriguing connection between $\langle QT\rangle$ and $\langle wT\rangle$, via which the lower bound of $\langle QT\rangle$ can be easily converted into the upper bound of $\langle wT\rangle$.

Furthermore, based on the inequality (7), a new bound of the vertical heat flux $\langle wT\rangle$ can be obtained as the following inequality:

$$F\left(g(1) - \langle wT\rangle\right) \ge \alpha g(1) - g(\alpha) - \alpha R^{-\frac{1}{3}} - \beta. \tag{19}$$

It should be noted that the analytical bounds derived above have an intriguing dependence on the Q-related term $g(1)$ whose value ranges in the interval $[0, 1]$, and $g(1) = 0$ and 1 correspond to the special heat source Q localized at the top and bottom walls, respectively.

3.3 Degradation to the UIHC

All the above theoretical results are obtained for the NUIHC. In the next, we consider the degraded situation, namely, the UIHC where the heat source is prescribed as $Q \equiv 1$. Because Q is a constant, the results obtained above can be greatly simplified.

Of importance, the lower bound of $\langle T\rangle$ is obtained via Eq. (7) as

$$\langle T\rangle \ge R^{-\frac{1}{3}}(1 - R^{-\frac{1}{3}}). \tag{20}$$

Equation (20) is formulated as the same derived by Lu et al. [31]. In the UIHC, one has $q_b = 1/2 - \langle wT\rangle$ (degraded from Eq. (13)). Therefore, Eq. (18) reduces to

$$\langle T\rangle \le \frac{1}{8} - \frac{1}{2}\langle wT\rangle^2, \tag{21}$$

which establishes an intrinsic link between the bounds of $\langle T\rangle$ and $\langle wT\rangle$ in an analytical way. Taking advantage of Eq. (21), the bound of $\langle T\rangle$ obtained by Lu et al. [31] (see Table 1), can be easily converted into the upper bound of $\langle wT\rangle$

$$\langle wT\rangle \le \left(\frac{1}{4} - 8.842R^{-\frac{1}{3}}\right)^{\frac{1}{2}}, \quad Pr \ne \infty. \tag{22}$$

Compared to the bounds given by Kumar et al. [34] and Arslan et al. [33], Eq. (22) provides an analytically stricter bound for $\langle wT\rangle$. This improved bound is indicated to increase asymptotically up to $1/2$ with a rate of $R^{-1/6}$, also recovering the bound obtained by Goluskin and Spiegel [14] as R is increased sufficiently high.

4. Numerical simulations

4.1 Simulation set-up

To demonstrate the analytical analysis derived above, numerical simulations are performed using an open-source CFD solver, buoyantBoussinesqPimpleFoam, in OpenFOAM [41, 42] which is based on the unstructured finite volume method. The PIMPLE algorithm that combines the PISO and SIMPLE (SIMPLEC) algorithms has been incorporated into this solver for the pressure-velocity coupling. A second-order implicit backward differencing scheme is employed for the discretization of the temporal term and a second-order central differencing scheme for the convection terms and diffusion terms [41, 42].

The code validations are conducted extensively in Appendix B. As the simplified cases of the NUIHC, two-dimensional (2-D) numerical simulations are performed following Golusking and van der Poel [13], with the computational size $L_x = 4d$ chosen along with a grid size of $N_x \times N_z = 380 \times 160$. Typically, the Rayleigh number is fixed at $R = 10^7$ and the Prandtl number is $Pr = 1$. The convection is assured to achieve the fully developed (statistically stationary) states when $\langle T \rangle$ obtains a time variation less than 0.5%.

Without loss of generality, the non-uniform heat resources are chosen to be z-dependent-only functions, i.e., $Q(z)$. Specifically, we design to use two representative families of functions as illustrated in Fig. 2. The family 1 is composed of continuous functions taking the forms expressed in

$$Q_{1,j}(z) = \begin{cases} n_j z^{n_j-1}, & j \le 4, \\ n_j (1-z)^{n_j-1}, & j \ge 5, \end{cases} \tag{23}$$

where $n_j = \{11, 7, 4, 2, 1, 2, 4, 7, 11\}$ in sequence for $j = 1, 2, ..., 9$. The family 2 is composed of step functions taking the forms expressed in

$$Q_{2,j}(z) = \begin{cases} \dfrac{1}{1-m_j}, & z \ge m_j, \\ 0, & z < m_j, \end{cases} \quad j \le 4, \tag{24a}$$

$$Q_{2,j}(z) = \begin{cases} \dfrac{1}{m_j}, & z \le m_j, \\ 0, & z > m_j, \end{cases} \quad j \ge 5, \tag{24b}$$

where $m_j = \left\{\frac{19}{20}, \frac{9}{10}, \frac{4}{5}, \frac{1}{2}, 1, \frac{1}{2}, \frac{1}{5}, \frac{1}{10}, \frac{1}{20}\right\}$ in sequence for $j = 1, 2, ..., 9$. In the following, $Q_{i,1}$-$Q_{i,9}$ ($i = 1, 2$), are used to represent the members of each family in order.

4.2 Choice of $Q(z)$

As seen in Fig. 2, $Q_{i,1}$-$Q_{i,9}$ ($i = 1, 2$) correspond to a series of heat sources which are highly localized in the vertical direction, namely, from being localized near the top wall ($Q_{i,1}$) to near the bottom wall ($Q_{i,9}$). Firstly, these types of $Q(z)$ represent the simplified heat source from some natural or industrial problems [4, 5]. In addition, this design of such families of heat sources yields typical sample values of the Q-related term $g(1)$ in the interval $[0, 1]$, standing for different NUIHC flows. In that, it is rational to demonstrate the analytical bounds derived in Sect. 3 based on the numerical results obtained for these two families of heat sources.

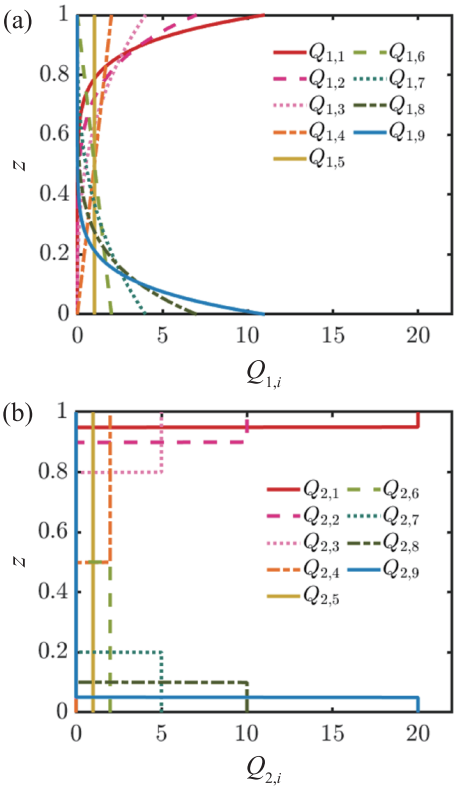

Figure 2 The z-dependent heat source distributions described as family 1 (a) and family 2 (b).

4.3 Numerical results

Figures 3 and 4 show the instantaneous temperature fields obtained via numerical simulations for typical heat sources of family 1 and family 2, respectively. Correspondingly, the averaged temperature rescaled as $\overline{T}/\overline{T}_{\mathrm{st}}$ are plotted in Fig. 5. Previous studies have indicated a clear correlation between flow structures and heat transfer efficiency [43]. In NUIHC, of interest, the flow structures also depend on the distribution of heat sources. One should note that when the heat sources are mainly concentrated closer to the top wall ($Q_{i,1}$), more heat will directly escape through the top wall and the fluid therefore remains cold and even stationary, especially in the bottom wall region. In this situation, the NUIHC is not well

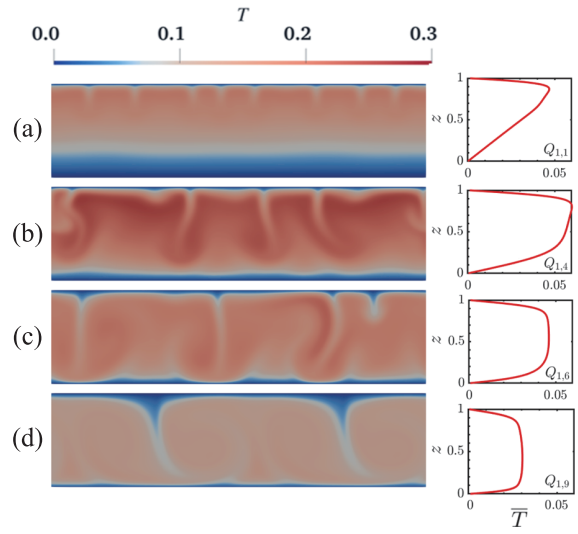

Figure 3 (a)-(d) Instantaneous temperature field obtained for heat source $Q_{1,1}, Q_{1,4}, Q_{1,6}, Q_{1,9}$ of family 1.

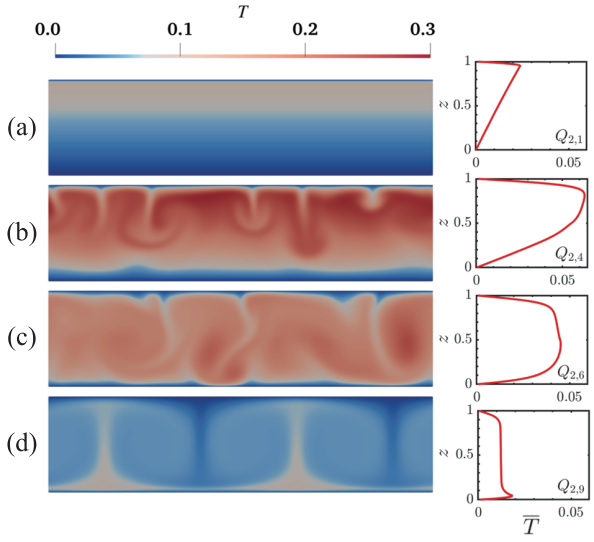

Figure 4 (a)-(d) Instantaneous temperature field obtained for heat source $Q_{2,1}, Q_{2,4}, Q_{2,6}, Q_{2,9}$ of family 2.

energized (penetrating vertically across the fluid layer) so it imposes a very weak impact on the lower half of the fluid layer where it has a stable stratification, for example, see Figs. 3(a) and 4(a). Consequently, the profiles of $\overline{T}/\overline{T}_{\rm st}$ are close to 1, particularly within the region of a stable stratification, as plotted in Fig. 5 for $Q_{i,1}$.

As the heat sources are more spreading vertically leading to an extending in the upper layer of an unstable stratification, for example, $Q_{2,4}$ and $Q_{2,6}$, convection occurs more energetically resulting in well mixing of the hot fluid in the bulk (see Fig. 4(b) and (c)). Therefore, the profile of the $\overline{T}$ in the bulk region obtains an obvious increase, causing a rapid decline when rescaled as $\overline{T}/\overline{T}_{\rm st}$ in Fig. 5(b). For the case of $Q_{2,4}$ which corresponds to most of the heat source spreading only

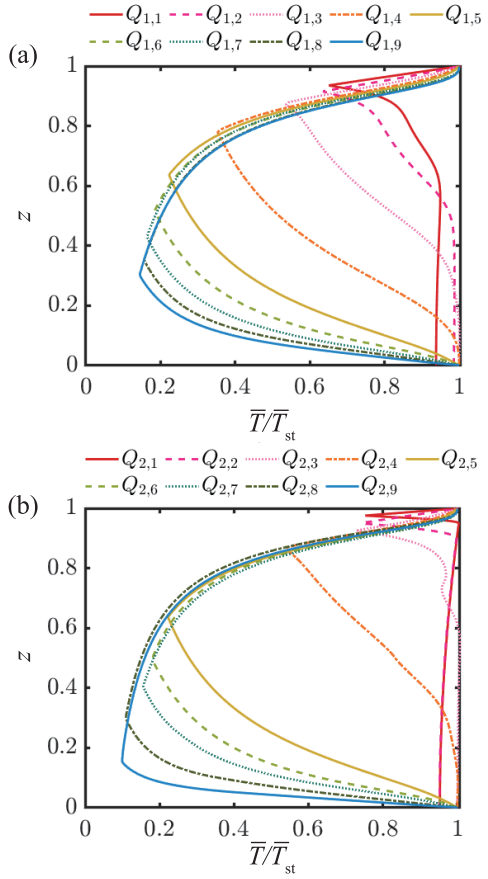

Figure 5 Profiles of the averaged temperature rescaled as $\overline{T}/\overline{T}_{\rm st}$ for different heat sources of family 1 (a) and family 2 (b).

in the upper half of the fluid layer, the thermal boundary layer near the bottom wall is still considerably thick and of stable stratification, see Fig. 4(b). The values of $\overline{T}/\overline{T}_{\rm st}$ in the lower stably stratified layer remain close to 1. For the case of $Q_{2,6}$, as the heat source is prescribed to exist only in the lower half of the fluid layer, enhanced convection emerges with the plumes almost penetrating the entire fluid layer, leading to the thinning of the thermal boundary layer near the bottom wall where it is even of stable stratification, see Fig. 4(c).

When the heat source is prescribed highly localized immediately close to the bottom wall (for example, $Q_{2,9}$), convective flow is driven to penetrate the whole fluid layer as it becomes almost fully unstably stratified and thus this NUIHC behaves reminiscent of the classic RBC that is heated by the hot bottom wall. As seen in Fig. 4(d), the large-scale circulations appear to dominate the entire fluid layer, a characteristic flow pattern of the classic RBC, even though most of the fluid layer is absent of heat source. As a consequence, the profiles of $\overline{T}/\overline{T}_{\rm st}$ are similarly shaped for $Q_{i,5}$-$Q_{i,9}$, as shown in Fig. 5. Note that, the value of $\overline{T}/\overline{T}_{\rm st}$ is always not greater than 1 for all the heat sources considered in the present simulations, which demonstrates that Eq. (14) is acceptably reasonable.

Figure 6 shows the comparison between $\langle T \rangle$ and $\langle T_{\rm st} \rangle$ for

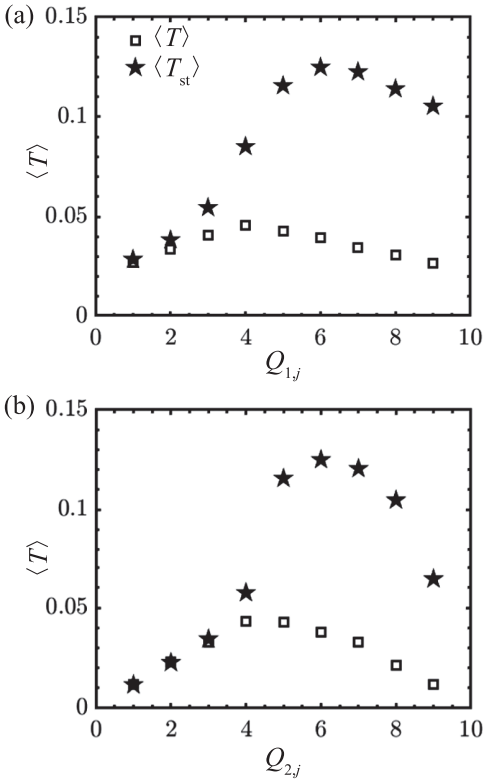

Figure 6 Comparison of $\langle T\rangle$ and the corresponding $\langle T_{\rm st}\rangle$ for different heat sources: (a) $Q_{1,j}$ of family 1; (b) $Q_{2,j}$ of family 2.

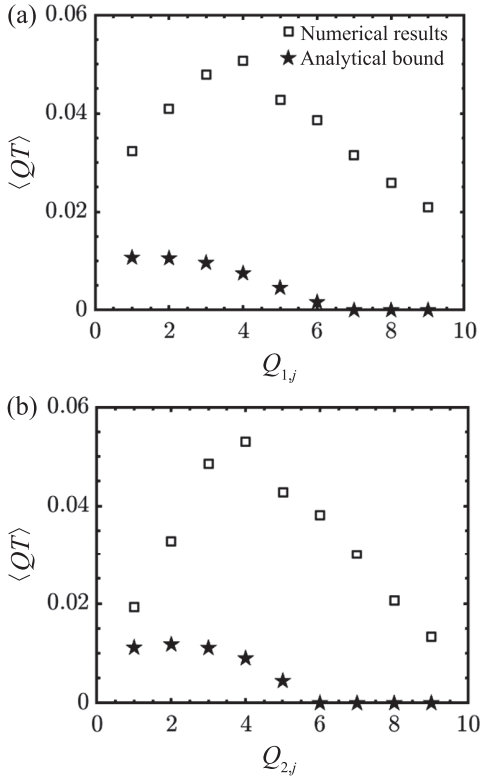

Figure 7 Comparison of $\langle QT\rangle$ and the corresponding lower bound (Eq. (7)) for different heat sources: (a) $Q_{1,j}$ of family 1; (b) $Q_{2,j}$ of family 2.

different heat sources of both family 1 and family 2, which also confirms the rationality of the assumption $\langle T\rangle \le \langle T_{\rm st}\rangle$. It is seen that the disparity between $\langle T\rangle$ and $\langle T_{\rm st}\rangle$ is small when the heat sources are concentrated near the top wall (namely, $Q_{1,j}$ and $Q_{2,j}$ with $j = 1, 2$), causing that the flow is not well energized and thus almost stationary. When the heat sources become more localized and closer to the bottom wall, namely, for $Q_{1,j}$ and $Q_{2,j}$ with $j > 3$, convection is strengthened enhancing the heat transfer efficiency of the fluid layer. In that, the fluid layer is maintained to have a decrease in $\langle T\rangle$ which obtains greater deviation from $\langle T_{\rm st}\rangle$ compared to the cases of $Q_{1,j}$ and $Q_{2,j}$ with $j = 1, 2$. This underscores that the analytical bound we derived works more stringently as the heat sources are localized near the top wall and the flow remains almost stationary.

Figures 7 and 8 show the comparisons between the numerical results and the analytical bounds of $\langle QT\rangle$ (Eq. (7)) and $\langle wT\rangle$ (Eq. (19)), respectively, in order to validate these two bounds. As shown in Fig. 7, the analytic lower bound of $\langle QT\rangle \ge 0$ presents a reasonable prediction, i.e., it obtains values smaller than those predicted as real values of the NUIHC by numerical simulations. Specifically, as the heat source is changed from be localized near the top wall to be uniformly distributed in the fluid layer ($Q_{i,1}$-$Q_{i,5}$ with $i = 1, 2$), non-zero bound values of $\langle QT\rangle$ are obtained according to Eq. (7),

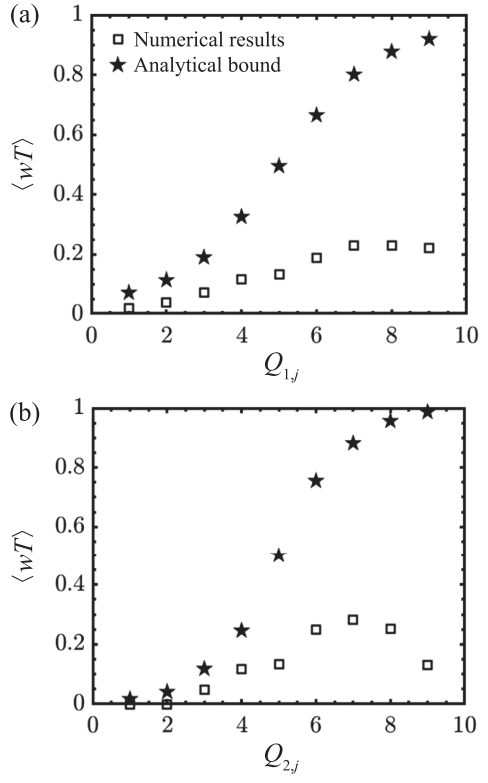

Figure 8 Comparison of $\langle wT\rangle$ and the corresponding upper bound (Eq. (19)) for different heat sources: (a) $Q_{1,j}$ of family 1; (b) $Q_{2,j}$ of family 2.

demonstrating a trend qualitatively agree with the numerical results. However, nearly zero bound values are obtained by Eq. (7) for $Q_{i,6}$-$Q_{i,9}$, indicating the present analytical bound recovers the uniform bound $\langle QT\rangle \geq 0$ as the heat source becomes localized closer to the bottom wall and consequently convection is more energized. In Fig. 8, the analytical bound of $\langle wT\rangle$ is shown to increase monotonically with $Q_{i,1} \to Q_{i,9}$ whereas the numerical results demonstrate a non-monotonic behavior. It presents a significant overestimation of the upper bound of $\langle wT\rangle$ when the heat sources are distributed near the bottom wall. In this sense, Eq. (19) yields acceptable upper bound values for the NUIHC as they are all greater than the real values obtained by numerical simulations.

5. Conclusions

The bounds of the temperature and the vertical heat flux in the NUIHC are studied via analytical analysis and numerical simulations in the present work. Specifically, the temperature bounds are analytically derived for the first time using the background method and obtained as inequalities of the weighted average temperature $\langle QT\rangle$ and the root-mean-square temperature $\langle T^2\rangle^{\frac{1}{2}}$ for the arbitrary heat source Q and finite Pr. Of physical importance, a novel inequality connecting $\langle QT\rangle$ and the average vertical heat flux $\langle wT\rangle$ is established, which works as an intrinsic relation to convert the lower bound of $\langle QT\rangle$ into the upper bound of $\langle wT\rangle$. The above analytical bounds are verified to degrade to the UIHC situations, yielding an analytically stricter bound of $\langle wT\rangle$, namely $\langle wT\rangle \leq (\frac{1}{4} - 8.842R^{-\frac{1}{3}})^{\frac{1}{2}}$ for finite Pr, by using of the upper bound given by Lu et al. [31]. A series of numerical simulations are conducted with two representative families of Q to comprehensively validate the analytical bounds. By comparing with numerical results, it is found the analytical bounds derived in the present work yield more reasonable predictions as the heat source is localized closer to the top wall leading to weak convection.

It should be pointed out that there are still some limitations in our work. First, the derivation of the bound of $\langle QT\rangle$ is based on the spatially-temporally averaged governing equations, which relaxes the constraints of the original partial differential equations (N-S equations) and therefore expands the function space of the physical solutions. As a result, the real bound is expected to be contained by the analytical bound we obtained. Second, we chose a piecewise linear function as the background temperature profile for simplifications and assigned special values to the undetermined parameters a, b, Δ_1 and Δ_2, rather than optimizing the background temperature profile to achieve the most stringent bounds. Third, the use of Eq. (14) further amplifies the upper bound of $\langle wT\rangle$. It is expected that the analytical bounds for the NUIHC can be further improved by addressing these issues in future work.

Appendix A. Derivation of the bound of $\langle QT\rangle$

The following is the analytical derivation of inequality Eq. (7) using the background method. First, taking the temporal-horizontal average of Eq. (1a) yields

$$\frac{\mathrm{d}\overline{w}}{\mathrm{d}z} = 0. \tag{A1}$$

With the no-penetration boundary conditions on the walls, one obtains $\overline{w} = 0$.

Then, the temperature field $T(x, y, z, t)$ is decomposed into a time-independent background profile $\tau(z)$ and a fluctuating part $\theta(x, y, z, t)$:

$$T(x, y, z, t) = \tau(z) + \theta(x, y, z, t). \tag{A2}$$

The boundary conditions of $\tau(z)$ and $\theta(x, y, z, t)$ at the walls are given as

$$\tau(0) = \tau(1) = \theta(x, y, 0, t) = \theta(x, y, 1, t) = 0. \tag{A3}$$

With the above decomposition, Eq. (1b) and (1c) become

$$Pr^{-1}(\partial_t \boldsymbol{u} + \boldsymbol{u}\cdot\nabla\boldsymbol{u} + \nabla p) = \nabla^2\boldsymbol{u} + R\tau\boldsymbol{e}_z + R\theta\boldsymbol{e}_z, \tag{A4a}$$

$$\partial_t\theta + \boldsymbol{u}\cdot\nabla\theta = \nabla^2\theta + Q + \tau'' - w\tau'. \tag{A4b}$$

As Pr is considered to be finite, taking the average of $\boldsymbol{u}\cdot$ (A4a) yields

$$\langle|\nabla\boldsymbol{u}|^2\rangle = R\langle w\theta\rangle. \tag{A5}$$

Similarly, the averaging of $\theta\times$ (A4b) and $\tau\times$ (A4b) yields

$$\langle w\theta\tau'\rangle = -\langle|\nabla\theta|^2\rangle - \langle\tau'\partial_z\theta\rangle + \langle Q\theta\rangle, \tag{A6a}$$

$$-\langle w\theta\tau'\rangle = -\langle\tau'\partial_z\theta\rangle + \langle Q\tau\rangle - \langle\tau'^2\rangle. \tag{A6b}$$

As $\langle T\rangle = \langle\tau\rangle + \langle\theta\rangle$, the difference between (A6a) and (A6b) is obtained as

$$\langle QT\rangle = \langle|\nabla\theta|^2\rangle + 2\langle w\theta\tau'\rangle + 2\langle Q\tau\rangle - \langle\tau'^2\rangle. \tag{A7}$$

We define

$$\begin{aligned} H &= \langle|\nabla\theta|^2\rangle + 2\langle\tau' w\theta\rangle \\ &= \langle|\nabla\theta|^2\rangle + \langle(2\tau' - a)w\theta\rangle + \frac{a}{R}\langle|\nabla\boldsymbol{u}|^2\rangle, \end{aligned} \tag{A8}$$

where a is an adjusting positive parameter. If $H \geq 0$, one obtains the lower bound of $\langle QT\rangle$ as

$$\langle QT\rangle = 2\langle Q\tau\rangle - \langle\tau'^2\rangle + H \geq 2\langle Q\tau\rangle - \langle\tau'^2\rangle. \tag{A9}$$

So we now turn to prove the existence of proper τ and a that ensures $H \geq 0$. Here we choose a piecewise linear background profile, as done by Lu et al. [31].

$$\tau = \begin{cases} \left(\frac{a}{2} + \frac{b}{\Delta_0}\right) z, & 0 \leq z < \Delta_0, \\ \frac{a}{2} z + b, & \Delta_0 \leq z < 1 - \Delta_1, \\ -\left[\frac{a}{2}\left(\frac{1}{\Delta_1} - 1\right) + \frac{b}{\Delta_1}\right](z-1), & 1 - \Delta_1 \leq z \leq 1, \end{cases} \tag{A10}$$

where Δ_0 and Δ_1 are the thicknesses of the boundary layer close to $z = 0$ and $z = 1$, respectively, and a and b are nonnegative parameters to be determined.

Then using the following inequality [36,44]:

$$\left| \int_0^{\Delta_0} \overline{wT} \mathrm{d}z \right| \leq \frac{\Delta_0^2}{4} \left[\frac{c}{4} \langle |\nabla \boldsymbol{u}|^2 \rangle + \frac{1}{c} \langle |\nabla \theta|^2 \rangle \right], \tag{A11}$$

where $c > 0$, the nonlinear term $\langle (2\tau' - a) w\theta \rangle$ in Eq. (A8) can be estimated by

$$\begin{aligned} |\langle (2\tau' - a) w\theta \rangle| \leq & \frac{b\Delta_0}{2} \left[\frac{c_1}{4} \langle |\nabla \boldsymbol{u}|^2 \rangle + \frac{1}{c_1} \langle |\nabla \theta|^2 \rangle \right] \\ & + \frac{(a+2b)\Delta_1}{4} \left[\frac{c_2}{4} \langle |\nabla \boldsymbol{u}|^2 \rangle + \frac{1}{c_2} \langle |\nabla \theta|^2 \rangle \right], \end{aligned} \tag{A12}$$

where c_1 and c_2 are free parameters required to be positive. So the bound of H can be estimated as

$$\begin{aligned} H \geq & \left[1 - \frac{b\Delta_0}{2c_1} - \frac{(a+2b)\Delta_1}{4c_2} \right] \langle |\nabla \theta|^2 \rangle \\ & + \left[\frac{a}{R} - \frac{b\Delta_0 c_1}{8} - \frac{(a+2b)\Delta_1 c_2}{16} \right] \langle |\nabla \boldsymbol{u}|^2 \rangle. \end{aligned} \tag{A13}$$

A sufficient condition for H to be semidefinite is to let the two coefficients on the right-hand side of Eq. (A13) be nonnegative, namely,

$$\begin{cases} 1 - \frac{b\Delta_0}{2c_1} - \frac{(a+2b)\Delta_1}{4c_2} \geq 0, \\ \frac{a}{R} - \frac{b\Delta_0 c_1}{8} - \frac{(a+2b)\Delta_1 c_2}{16} \geq 0. \end{cases} \tag{A14}$$

Without loss of generality, we can set $c_1 = c_2 = c > 0$, and specify a and b as

$$\begin{cases} a = \Delta_1 - \Delta_0, \\ b = \frac{\Delta_0}{2}(1 - \Delta_1). \end{cases} \tag{A15}$$

In that, Eq. (A14) is reduced to

$$\begin{cases} 4c \geq \Delta_0^2(1 - \Delta_1) + \Delta_1^2(1 - \Delta_0), \\ \frac{64(\Delta_1 - \Delta_0)}{R} \geq [\Delta_0^2(1 - \Delta_1) + \Delta_1^2(1 - \Delta_0)]c. \end{cases} \tag{A16}$$

Only one feasible solution is needed for our problem. For simplicity, we can replace the inequality sign with an equality sign, and then it is easy to obtain

$$\frac{64(\Delta_1 - \Delta_0)}{R} = [\Delta_0^2(1 - \Delta_1) + \Delta_1^2(1 - \Delta_0)]^2. \tag{A17}$$

One can easily find that $\Delta_0 = 0$ and $\Delta_1^3 = \frac{64}{R}$ correspond to a feasible solution to satisfy $H \geq 0$. It indicates that there indeed exist proper τ and a that ensure $H \geq 0$. Using this special background temperature and defining $h(z) = \int_0^z \overline{Q}(z')\mathrm{d}z'$ and $g(z) = \int_0^z h(z')\mathrm{d}z'$, the bound of $\langle QT \rangle$ can be obtained as

$$\begin{aligned} \langle QT \rangle &\geq 2\langle Q\tau \rangle - \langle \tau'^2 \rangle \\ &= 2\int_0^1 \overline{Q}\tau \mathrm{d}z - \int_0^1 \tau'^2 \mathrm{d}z \\ &= 2(h\tau)|_0^1 - 2\int_0^1 h\tau' \mathrm{d}z - \int_0^1 \tau'^2 \mathrm{d}z \\ &= -2\left[\int_0^{\Delta_0^-} h\tau' \mathrm{d}z + \int_{\Delta_0^+}^{(1-\Delta_1)^-} h\tau' \mathrm{d}z \right. \\ &\quad \left. + \int_{(1-\Delta_1)^+}^1 h\tau' \mathrm{d}z \right] - \int_0^1 \tau'^2 \mathrm{d}z \\ &= -2\left[(g\tau')|_0^{\Delta_0^-} + (g\tau')|_{\Delta_0^+}^{(1-\Delta_1)^-} + (g\tau')|_{(1-\Delta_1)^+}^1 \right] \\ &\quad - \int_0^{\Delta_0} \tau'^2 \mathrm{d}z - \int_{\Delta_0}^{1-\Delta_1} \tau'^2 \mathrm{d}z - \int_{1-\Delta_1}^1 \tau'^2 \mathrm{d}z \\ &= -g(\Delta_0)\frac{2b}{\Delta_0} - g(1-\Delta_1)\frac{a+2b}{\Delta_1} \\ &\quad + 2g(1)\left[\frac{a}{2}\left(\frac{1}{\Delta_1} - 1 \right) + \frac{b}{\Delta_1} \right] - \frac{\Delta_1}{4}(1-\Delta_1) \\ &= g(1)(1-\Delta_1) - g(1-\Delta_1) - \frac{\Delta_1}{4}(1-\Delta_1) \\ &= g(1)(1 - 4R^{-\frac{1}{3}}) - g(1 - 4R^{-\frac{1}{3}}) \\ &\quad - R^{-\frac{1}{3}}(1 - 4R^{-\frac{1}{3}}). \end{aligned} \tag{A18}$$

By choosing appropriate values of Δ_0 and Δ_1, the right-hand side of Eq. (A18), namely, $2\langle Q\tau \rangle - \langle \tau'^2 \rangle$, will reach its maximum value under the constrain of $H \geq 0$. For the UIHC, optimization has been conducted by Lu et al. [31] to determine the appropriate values of Δ_0 and Δ_1, while it is quite challenging in the present NUIHC and would be one of the motivations for our future work. At this point, selecting the special values as $\Delta_0 = 0$ and $\Delta_1^3 = \frac{64}{R}$ is more practical, which leads Eq. (A18) to be reduced as

$$\langle QT \rangle \geq g(1)(1 - 4R^{-\frac{1}{3}}) - g(1 - 4R^{-\frac{1}{3}}) - R^{-\frac{1}{3}}(1 - 4R^{-\frac{1}{3}}). \tag{A19}$$

Hence, Eq. (7) is obtained.

Appendix B. Code validation

We first perform code validation via a series of 2D numerical simulations for the UIHC by changing the Rayleigh number as listed in Table B1 and fixing $Pr = 1$, for which the horizontal and vertical domain sizes are set as $L_x \times L_z = 4d \times d$ corresponding a grid size of 360×160. The q_b values obtained by the present simulations compare fairly well with those reported by Goluskin and van der Poel [13]. Furthermore, 3D numerical simulation is also performed for a typical case of $R = 10^7$, for which the computational domain is set as $L_x \times L_y \times L_z = 2d \times 2d \times d$ corresponding to a grid size of $128 \times 128 \times 128$. The grids are clustered in the wall-normal (y) direction near the top and bottom walls and kept uniform in x- and z-directions. The grid spacing grows linearly with a difference of 2.8×10^{-4} (2D cases) or 3.7×10^{-3} (3D cases), which is also the resolution of the first grid immediately close to the wall. 14 (3D cases) or 19 (2D cases) grids are placed within the thermal boundary layer, whose dimensionless thickness is estimated by $\langle T \rangle / [1/2 + \langle wT \rangle]$ [13]. The average Kolmogorov length scale can be estimated by $\eta = Pr^{1/2}/[R\langle wT \rangle]^{1/4}$ [13]. The ratio of the average Kolmogorov length scale to the maximum gird length ($\max\{\delta_x, \delta_y, \delta_z\}$) is 1.78 (for 3D cases) or 2.64 (for 2D cases). The ratio of the average Kolmogorov time scale, calculated by $\tau_\eta = \eta^2/\nu$, to the simulation time step is 78.6 (for 3D cases) or 98.2 (for 2D cases). So the current grid size and time step can adequately resolve the Kolmogorov scale in fully developed turbulent convection considered. In Fig. B1, the good agreement of the averaged temperature with that of Goluskin and van der Poel [13] further confirms that the present simulations based on OpenFOAM are reliable for producing the essential flow features of the NUIHC.

Table B1 Comparison of q_b with Goluskin and van der Poel [13]

R	David Goluskin	Present	Error (%)
10^6	0.403	0.412	2.25
10^7	0.360	0.363	0.83
10^8	0.335	0.336	0.30

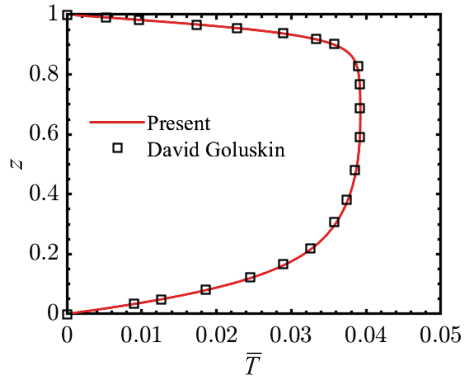

Figure B1 Profile of the averaged temperature obtained by OpenFOAM, compared with Goluskin and van der Poel [13] for $R = 10^7$.

Conflict of interest *On behalf of all authors, the corresponding author states that there is no conflict of interest.*

Author contributions *Liangbing Chen provided research concepts and overarching research goals, developed the methodology and conducted the research and investigation process. Liangbing Chen completed early work on theoretical derivation and numerical simulations. An-Kang Gao and Zimo Liao helped to conduct the investigation process and expanded the theoretical derivation. Zhenhua Wan and Zimo Liao repeatedly checked and validated the theoretical derivation process and numerical simulations. Liangbing Chen presented the published work and visualized the simulation data. Liangbing Chen and An-Kang Gao wrote the first draft of the manuscript. An-Kang Gao and Nansheng Liu revised and edited the final version, and supervised the advancement of the research. Nansheng Liu provided the computing resources and financial support for the research.*

Acknowledgements *The work was supported by the National Natural Science Foundation of China (Grant Nos. 92252202, 92152301, 12293000, 12293002, 12302320, and 12388101), and the Fundamental Research Funds for the Central Universities. The authors thank X.-Y. Lu for many useful and illuminating discussions.*

1 Y. Du, M. Zhang, and Y. Yang, Thermal convection driven by a heat-releasing scalar component, Acta Mech. Sin. **38**, 321584 (2022).
2 Y. Yang, Double diffusive convection in the finger regime for different Prandtl and Schmidt numbers, Acta Mech. Sin. **36**, 797 (2020).
3 G. Schubert, D. L. Turcotte, and P. Olson, Mantle Convection in the Earth and Planets (Cambridge University Press, Cambridge, 2001).
4 R. Kippenhahn, A. Weigert, and A. Weiss, Stellar Structure and Evolution (Springer, Berlin, Heidelberg, 1990).
5 K. A. Emanuel, Atmospheric Convection (Oxford University Press, Oxford, 1994).
6 Y. Shen, and O. Zikanov, Thermal convection in a liquid metal battery, Theor. Comput. Fluid Dyn. **30**, 275 (2016), arXiv: 1507.08315.
7 Z. Lu, G. Liu, and B. Wang, Flow structure and heat transfer of electro-thermo-convection in a dielectric liquid layer, Phys. Fluids **31**, 064103 (2019).
8 D. J. Tritton, and M. N. Zarraga, Convection in horizontal layers with internal heat generation. Experiments, J. Fluid Mech. **30**, 21 (1967).
9 A. Limare, C. Jaupart, E. Kaminski, L. Fourel, and C. G. Farnetani, Convection in an internally heated stratified heterogeneous reservoir, J. Fluid Mech. **870**, 67 (2019).
10 F. A. Kulacki, and R. J. Goldstein, Thermal convection in a horizontal fluid layer with uniform volumetric energy sources, J. Fluid Mech. **55**, 271 (1972).
11 V. Bouillaut, S. Lepot, S. Aumaître, and B. Gallet, Transition to the ultimate regime in a radiatively driven convection experiment, J. Fluid Mech. **861**, R5 (2019), arXiv: 2010.10936.
12 Y. Tasaka, and Y. Takeda, Effects of heat source distribution on natural convection induced by internal heating, Int. J. Heat Mass Transfer **48**, 1164 (2005).
13 D. Goluskin, and E. P. van der Poel, Penetrative internally heated convection in two and three dimensions, J. Fluid Mech. **791**, R6 (2016), arXiv: 1511.05966.
14 D. Goluskin, and E. A. Spiegel, Convection driven by internal heating, Phys. Lett. A **377**, 83 (2012), arXiv: 1210.8154.
15 Z. L. Xia, C. B. Zhao, J. Z. Wu, B. F. Wang, and K. L. Chong, Temperature response to periodic modulation in internal heating convection, Phys. Fluids **34**, 125133 (2022).

16 C. Jain, and V. S. Solomatov, Onset of convection in internally heated fluids with strongly temperature-dependent viscosity, Phys. Fluids **34**, 096604 (2022).
17 G. Kefayati, Internally heated convection of viscoplastic fluids in enclosures using a lattice Boltzmann method, Phys. Fluids **35**, 013108 (2023).
18 Q. Wang, D. Lohse, and O. Shishkina, Scaling in internally heated convection: A unifying theory, Geophys. Res. Lett. **48**, e2020GL091198 (2021), arXiv: 2010.05789.
19 D. Goluskin, Internally Heated Convection and Rayleigh-Bénard Convection (Springer, Berlin, 2016).
20 A. J. Harfash, Three dimensional simulations of penetrative convection in a porous medium with internal heat sources, Acta Mech. Sin. **30**, 144 (2014).
21 A. Mahajan, and M. K. Sharma, Penetrative convection in magnetic nanofluids via internal heating, Phys. Fluids **29**, 034101 (2017).
22 X. He, and P. Tong, Space-time correlations in turbulent Rayleigh-Bénard convection, Acta Mech. Sin. **30**, 457 (2014).
23 H. Y. Zou, W. F. Zhou, X. Chen, Y. Bao, J. Chen, and Z. S. She, Boundary layer structure in turbulent Rayleigh-Bénard convection in a slim box, Acta Mech. Sin. **35**, 713 (2019), arXiv: 1901.07913.
24 X. Zhu, and Q. Zhou, Flow structures of turbulent Rayleigh-Bénard convection in annular cells with aspect ratio one and larger, Acta Mech. Sin. **37**, 1291 (2021).
25 I. Tobasco, D. Goluskin, and C. R. Doering, Optimal bounds and extremal trajectories for time averages in nonlinear dynamical systems, Phys. Lett. A **382**, 382 (2018), arXiv: 1705.07096.
26 G. Fantuzzi, A. Arslan, and A. Wynn, The background method: Theory and computations, Phil. Trans. R. Soc. A. **380**, 20210038 (2022), arXiv: 2107.11206.
27 G. Fantuzzi, and A. Wynn, Optimal bounds with semidefinite programming: An application to stress-driven shear flows, Phys. Rev. E **93**, 043308 (2016), arXiv: 1512.05615.
28 C. R. Doering, F. Otto, and M. G. Reznikoff, Bounds on vertical heat transport for infinite-Prandtl-number Rayleigh-Bénard convection, J. Fluid Mech. **560**, 229 (2006).
29 S. Chernyshenko, Relationship between the methods of bounding time averages, Phil. Trans. R. Soc. A. **380**, 20210044 (2022).
30 D. Goluskin, and G. Fantuzzi, Bounds on mean energy in the Kuramoto-Sivashinsky equation computed using semidefinite programming, Nonlinearity **32**, 1705 (2019), arXiv: 1802.08240.
31 L. Lu, C. R. Doering, and F. H. Busse, Bounds on convection driven by internal heating, J. Math. Phys. **45**, 2967 (2004).
32 A. Arslan, G. Fantuzzi, J. Craske, and A. Wynn, Bounds on heat transport for convection driven by internal heating, J. Fluid Mech. **919**, A15 (2021), arXiv: 2102.06458.
33 A. Arslan, G. Fantuzzi, J. Craske, and A. Wynn, Rigorous scaling laws for internally heated convection at infinite Prandtl number, J. Math. Phys. **64**, 023101 (2023), arXiv: 2205.03175.
34 A. Kumar, A. Arslan, G. Fantuzzi, J. Craske, and A. Wynn, Analytical bounds on the heat transport in internally heated convection, J. Fluid Mech. **938**, A26 (2022), arXiv: 2110.10344.
35 J. P. Whitehead, and C. R. Doering, Internal heating driven convection at infinite Prandtl number, J. Math. Phys. **52**, 093101 (2011), arXiv: 1104.2792.
36 C. R. Doering, and P. Constantin, Variational bounds on energy dissipation in incompressible flows. III. Convection, Phys. Rev. E **53**, 5957 (1996).
37 G. Fantuzzi, A. Arslan, and A. Wynn, The background method: Theory and computations, Phil. Trans. R. Soc. A. **380**, 20210038 (2022), arXiv: 2107.11206.
38 Y. Zhang, Q. Zhou, and C. Sun, Statistics of kinetic and thermal energy dissipation rates in two-dimensional turbulent Rayleigh-Bénard convection, J. Fluid Mech. **814**, 165 (2017).
39 Y. Wang, W. Xu, X. He, H. Yik, X. Wang, J. Schumacher, and P. Tong, Boundary layer fluctuations in turbulent Rayleigh-Bénard convection, J. Fluid Mech. **840**, 408 (2018).
40 A. Xu, L. Shi, and H. D. Xi, Statistics of temperature and thermal energy dissipation rate in low-Prandtl number turbulent thermal convection, Phys. Fluids **31**, 125101 (2019), arXiv: 1911.04042.
41 J. Höpken, and K. G. Mooney, The openfoam® technology primer, 2021.
42 C. J. Greenshields, OpenFOAM v6 User Guide (OpenFOAM Foundation Ltd., London, 2015).
43 A. Xu, X. Chen, F. Wang, and H. D. Xi, Correlation of internal flow structure with heat transfer efficiency in turbulent Rayleigh-Bénard convection, Phys. Fluids **32**, 105112 (2020), arXiv: 2009.07675.
44 R. Rosa, and R. Temam, Optimal minimax bounds for time and ensemble averages of dissipative infinite-dimensional systems with applications to the incompressible navier-stokes equations, arXiv: 2010.06730.

非均匀内部热源驱动对流的温度和热通量界

陈良兵, 高安康, 廖紫默, 万振华, 刘难生

摘要 通过理论分析和数值模拟研究了两个水平等温壁面之间受非均匀内部热源驱动的对流, 以探索温度和数值热通量的界. 具体而言, 通过将温度分解为定常的背景温度剖面和脉动温度两部分, 解析地推导出了加权平均温度$\langle QT\rangle$的严格下界. 作为首个考虑非均匀内部热源的解析界, 它能与已有的用于均匀内部加热对流的界兼容. 更具物理意义的是, 通过使用下壁面平均热通量(q_b)作为中间变量, 我们得到了一个解析关系用于构建$\langle QT\rangle$和平均竖直热通量$\langle wT\rangle$的不等关系. 它揭示了$\langle QT\rangle$的下界和$\langle wT\rangle$的上界之间的内在关联, 即这两个界本质上是等价的, 它提供了一种简单的方法将一个界转化为另一个. 此外，我们通过一系列全面的数值模拟，对解析界进行了广泛的测试验证.